Model-Based Interpretation of PolSAR Data for the Characterization of Glacier Zones in Greenland

Journal Article

Author(s):
Parrella, Giuseppe; Hajnsek, Irena; Papathanassiou, Konstantinos

Model-Based Interpretation of PolSAR Data for the Characterization of Glacier Zones in Greenland

Giuseppe Parrella 🔗, Irena Hajnsek 🔗, *Fellow, IEEE*, and Konstantinos P. Papathanassiou 🔗, *Fellow, IEEE*

Abstract—Different approaches have been proposed in recent years to map glacier zones using Synthetic Aperture Radar (SAR). Most of them rely on empirical or statistical approaches for the interpretation of backscatter intensity measurements and their seasonal variations related to the melting regime of the different glacier zones. This article focuses on the potential of polarimetric SAR measurements to characterize the scattering in the different glacier zones in order to distinguish between them. For this, a general two-component scattering model is proposed, accounting for surface and subsurface contributions in the different glacier zones. The (anisotropic) propagation through snow, firn, and ice layers is also accounted for as it plays an important role in the interpretation of the polarimetric signatures. A set of five polarimetric descriptors is proposed to describe the projection of the model on the SAR measurements. The ability of the model to characterize the scattering in the different glacier zones is validated and discussed at different frequencies (X-, C-, and L-band). For this, a multi-frequency airborne SAR dataset acquired by the DLR's F-SAR sensor in West Greenland during the ARCTIC 2015 campaign is used. The achieved results indicate that L-band polarimetric measurements allow to differentiate the different glacier zones based on the subsurface (e.g., volume) scattering characteristics. In contrast, the increased (back-) scattering complexity and the reduced penetration capability limit the potential of X- and C-band polarimetric measurements.

Index Terms—Firn line, glacier zones, Greenland, polarimetric synthetic aperture radar (SAR), polarization phase difference.

I. INTRODUCTION

SURFACE mass balance represents a primary term of the total mass balance of a glacier or ice sheet. It is defined as the annual difference between the mass gained and lost due to surface processes, such as snow accumulation, melting and refreezing, and melt-water run-off. The spatial variability of the intensity of such phenomena (e.g., decreasing melt at increasing altitude) leads to the formation of glacier zones characterized by different surface and subsurface structure. The mapping of such zones is of high interest since their spatial extent and temporal variation are directly related to the surface mass balance.

Glaciers and ice sheets are generally divided into two main zones: the accumulation zone, where ice mass is gained, and the ablation zone, where mass is getting lost. The equilibrium line (EL) ideally separates the two zones at the altitude where the net mass balance is zero. Within the accumulation zone, up to three different subzones can be distinguished, according to the intensity of summer melt: 1) the dry snow zone, located at higher elevations, where no melt occurs and snow accumulates over time, becoming gradually denser with depth, transforming into firn and finally ice; 2) the percolation zone, located at lower altitudes, where occasional melting causes the percolation of liquid water and the formation of refrozen inclusions (ice lenses and pipes) into subsurface snow and firn layers; 3) the superimposed ice zone, the lowest part of the accumulation zone, characterized by substantial melting of the winter snowpack, which runs-off or refreezes at the surface forming ice layers [1]. The percolation and superimposed ice zones are ideally divided by the firn line (FL), which indicates the lowest location where firn is found. The location of the FL can be interpreted as an indicator of time-integrated surface mass balance changes [1].

The contribution of Synthetic Aperture Radar (SAR) measurements to the estimation of glacier mass balance is nowadays well established. Especially interferometric SAR (InSAR) techniques are widely used to accurately measure surface elevation changes and flow velocities [2]–[7]. Beyond this, the potential to distinguish and map glacier zones using SAR data was already recognized in the early days of SAR glacier research, primarily linking single-polarization backscatter coefficients to subsurface features [8], [9], [10]. Time series of ERS-1 data were exploited in [11] to mosaic backscattering coefficients over the whole Greenland, generating a first radar map of the ice sheet. Summer and winter ERS acquisitions were analyzed in [12] in order to characterize glaciological and geomorphological structures within the glacier zones. Multitemporal ERS acquisitions were employed in [13] to assess the sensitivity of backscattering coefficients to the zonation and the seasonal changes of glaciers in Svalbard, including an attempt to detect the FL as its annual change. Instead, the detection of the EL and its annual variations were proved to be more complex and only possible under specific conditions (e.g., dry snow and presence of superimposed ice) [14]. An approach based on the thresholding of winter C-band backscattering coefficients to retrieve firn masks and map the FL retreat on the Svartisen ice caps, Norway, over a 7-year period was proposed in [15]. With a similar approach, the FL retreat in the Norwegian Blamannsisen ice cap between 1992 and 2010 was mapped in [16]. Common to all studies is the difficulty in

detecting thin firn layers in the lowest part of the firn area, as they typically exhibit backscattering levels lower than thick firn but higher than bare/snow-covered ice. Late summer C-band backscattering images of the Qinghai–Tibetan Plateau, China, were employed in [17] to distinguish wet-snow/firn from bare ice, including an attempt to identify the thin firn boundary. In [18], a more advanced technique for FL monitoring was developed, based on statistical modeling of polarimetric covariance matrices. Recently, single-pass X-band interferometric coherence data from the TanDEM-X mission have been exploited to retrieve the zonation of the entire Greenland ice sheet [19].

The first multipolarization study based on the analysis of airborne multifrequency (C-, L-, and P-band) data was presented in 1993 [20]. Winter C- and L-band airborne polarimetric backscattering data of the Austre Okstindbreen glacier, Norway, were analyzed in [21], confirming the usefulness of polarimetry for glacier zones mapping. The study also confirmed the difficulties in detecting the annual EL, while a clear backscattering transition could be observed at the FL location.

To date, only few studies have addressed the modeling of PolSAR backscatter to gain a physical interpretation of polarimetric measurements of glaciers and ice sheets. The first model was presented in [22] to interpret C-, L-, and P-band data from the percolation zone of Greenland. Icy cylinders were modeled to describe the scattering behavior of ice lenses and pipes, which were considered to be the main sources of backscattering. Such scatterers were assumed to be embedded in a volume of non-scattering snow and firn, whose only effect is to refract the incident radar signal. Polarimetric phase differences observed in the data were interpreted as the result of multiple reflections occurring within the ice cylinders. The proposed model could describe satisfactorily the C-band data but could not fully explain the L- and P-band signatures. In [23], a three-component model was developed to interpret L- and P-band PolSAR backscattering from the percolation and superimposed ice zone of the Austfonna ice cap. The different components accounted for surface scattering from a shallow snow/ice interface, a volume contribution from randomly oriented dipole-like inclusions embedded in background of snow/ice, and a component associated to the presence of oriented sastrugi fields at the glacier surface. Despite the higher complexity, the modeling only addressed the amplitude term of the polarimetric measurements and did not consider the phase signal.

Recent studies have shown that firn (and snow) properties can be retrieved by exploiting the phase (differences) of polarimetric SAR data [24], [25]. A physical model was proposed in [26] to link polarimetric *HH-VV* phase differences to the thickness and structural anisotropy of firn layers. The approach has also been employed for the retrieval of firn maps over two areas in the accumulation zone of the Austfonna ice cap, Svalbard [24].

In this article, the coherent signatures (including amplitude and phase information) of multifrequency polarimetric SAR data are interpreted by means of a two-component model that describes polarimetric scattering and propagation effects across the different glacier zones. The model formulation makes use of the new results and deeper understanding developed over the last years. It allows to use a set of polarimetric descriptors

to characterize the main scattering processes in the different glacier zones and, in turn, to retrieve insights about their subsurface structure. In Section II, the theory of SAR polarimetry and the PolSAR descriptors of relevance for the analysis are introduced. The model-based approach employed for the glacier zones' characterization is described in Section III. Section IV presents the study area and the available SAR dataset. Section V reports a detailed polarimetric analysis of the data based on the descriptors and scattering models introduced in Section II. Finally, conclusions and ideas for possible future developments are presented in Section VI.

II. SCATTERING AND PROPAGATION MODEL

Quad-polarimetric SAR system configurations allow the measurement of the full polarimetric scattering matrix $[S]$ and provide data with a higher information content than conventional single- or dual-polarized SAR configurations that measure only a single element or row of $[S]$. Single (deterministic) scatterers are fully described by $[S]$. However, when different scatterers (stochastically distributed) are present within the resolution cell—as in the general case of glacier scattering scenarios—second order descriptors are required for a full description. Such a descriptor is the polarimetric covariance $[C]$ matrix, defined by the spatial correlation of the cross-products of the elements of $[S]$ [27].

For glacier scenarios, a two-component scattering model, accounting for surface $[C_{Sur}]$ and subsurface $[C_{Sub}]$ contributions, allows to describe the polarimetric scattering in the different zones and at different frequencies [24]

$$[C] = [C_{Sur}] + \int_0^\infty \sigma(z) [P] [C_{Sub}] [P]^+ dz \qquad (1)$$

where $\sigma(z)$ is the vertical backscattering distribution in the subsurface volume, and $[P]$ is the propagation matrix that describes the propagation through the volume itself, accounting for both attenuation and phase shifts. The surface contribution $[C_{Sur}]$, if present, is in most cases a rough surface scattering contribution. The subsurface contribution $[C_{Sub}]$ consists, in the most general case, of the superposition of rough surface scattering at different depths (accounting for the presence of subsurface melt layers) and volume scattering accounting for three-dimensional distributed scatterers. In addition, a nonscattering snow layer on top of the surface layer may be present. The latter is not explicitly accounted in (1) and its effect will be discussed later.

Surface scattering occurs at the ice surface in the ablation and superimposed ice zones as well as at subsurface melt layers in the percolation zone. Based on [24], surface scattering at slightly rough surfaces can be described using the X-Bragg model [28], which accounts for cross-polarized backscattering induced by roughness. The corresponding covariance matrix $[C_{Sur}]$ is given by [28]

$$[C_{Sur}] = \begin{bmatrix} C_1 & 0 & C_2 \\ 0 & C_3 & 0 \\ C_2^* & 0 & C_4 \end{bmatrix} \qquad (2)$$
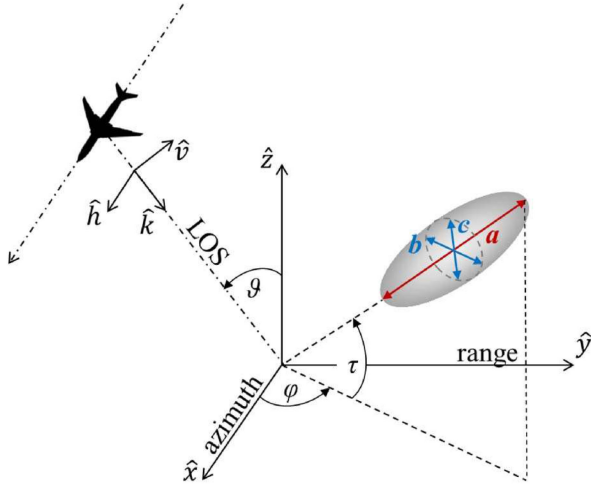
Fig. 1. Spheroidal particle in the $(\hat{x}, \hat{y}, \hat{z})$ reference system. The link to the radar reference frame $(\hat{h}, \hat{v}, \hat{k})$ is described by the incidence angle ϑ. $\hat{\mathrm{k}}$ is the propagation direction of the radar signal. *a, b, c,* with $b = c$, represent the axes of the spheroid along the *z*-, *x*-, and *y*-directions, respectively [24].

where

$$C_1 = 0.5 \left(g_1 + g_3 \left(1 + \mathrm{sinc}4\beta_1 \right) + \left(g_2^* + g_2 \right) \mathrm{sinc}2\beta_1 \right) \quad (3a)$$

$$C_2 = 0.5 \left(g_1 - g_3 \left(1 + \mathrm{sinc}4\beta_1 \right) + \left(g_2^* - g_2 \right) \mathrm{sinc}2\beta_1 \right) \quad (3b)$$

$$C_3 = g_3 \left(1 - \mathrm{sinc}4\beta_1 \right) \quad (3c)$$

$$C_4 = 0.5 \left(g_1 + g_3 \left(1 + \mathrm{sinc}4\beta_1 \right) - \left(g_2^* + g_2 \right) \mathrm{sinc}2\beta_1 \right). \quad (3d)$$

The coefficients g_1, g_2, and g_3 are defined according to [28] as

$$g_1 = |B_{HH} + B_{VV}|^2 \quad (4a)$$

$$g_2 = \left(B_{HH} + B_{VV} \right) \left(B_{HH} - B_{VV} \right)^* \quad (4b)$$

$$g_3 = 0.5 |B_{HH} - B_{VV}|^2 \quad (4c)$$

where B_{HH} and B_{VV} are the Bragg scattering coefficients [28], which depend on the dielectric discontinuity at the air / ice interface and on the incidence angle ϑ, while β_1 is the parameter that controls the roughness. The validity of the X-Bragg model is, however, limited to surfaces characterized by roughness conditions described by $0° < \beta_1 < 90°$, corresponding to $ks < 1$, where $k = 2\pi/\lambda$ is the wavenumber (with λ being the wavelength of the employed radar signal) and s the rms height of the surface [28].

The volume component can be described by a 3-D distribution of scatterers embedded in a homogeneous ice or firn background. Each scatterer is modeled as a spheroid with major axis a and minor axes $b = c$. The shape can vary from prolate (needles) with $a > b = c$, through spheres for $a = b = c$, to oblate (disks) with $a < b = c$. Their orientation is described in the $(\hat{x}, \hat{y}, \hat{z})$ reference system by the Euler angles, namely the (particle) orientation (φ) and tilt (τ) angles (see Fig. 1). By accounting for the incidence angle ϑ, the elements of the scattering matrix of a single spheroid can be linked to the radar reference frame $(\hat{h}, \hat{v}, \hat{k})$ and expressed as [24]

$$S_{HH}^P = A_P \cos^2\tau \cos^2\varphi + \left(\sin^2\varphi + \sin^2\tau \cos^2\varphi \right) \quad (5a)$$

$$S_{VV}^P = A_P \left(\cos\tau \sin\varphi \cos\vartheta + \sin\tau \sin\vartheta \right) + \cos^2\varphi \cos^2\vartheta$$
$$+ \sin\tau \sin\varphi \cos\vartheta - \cos\tau \sin\vartheta \quad (5b)$$

$$S_{HV}^P = A_P \left(\cos^2\tau \cos\varphi \sin\varphi \cos\vartheta + \cos\tau \sin\tau \cos\varphi \sin\vartheta \right)$$
$$- \cos\varphi \sin\varphi \cos\vartheta$$
$$+ \sin^2\tau \cos\varphi \sin\varphi \cos\vartheta - \cos\tau \sin\tau \cos\varphi \sin\vartheta \quad (5c)$$

where A_P is the particle (scatterer) anisotropy given by the ratio of the particle polarisabilities and depends on the particle shape (expressed as the vertical-to-horizontal axis ratio $S_P = a/b$) and permittivity (i.e., dielectric constant) [29]

$$A_P = \frac{L_2 + \frac{1}{\varepsilon - 1}}{L_1 + \frac{1}{\varepsilon - 1}}. \quad (6)$$

For prolates, the function L_1 becomes

$$L_1 = \frac{1 - e^2}{e^2} \left(-1 + \frac{1}{2e} \ln \left(\frac{1 + e}{1 - e} \right) \right) \text{ with } e = \sqrt{1 - \frac{b^2}{a^2}} \quad (7a)$$

while for oblates

$$L_1 = \frac{1 - e^2}{e^2} \left(-1 + \frac{1}{e} \mathrm{atan}\left(e \right) \right) \text{ with } e = \sqrt{\frac{b^2}{a^2} - 1} \quad (7b)$$

and in both cases

$$L_2 = \frac{1}{2} \left(1 - L_1 \right). \quad (7c)$$

The volume covariance matrix $[C_{Vol}]$ is obtained by integrating the scattering matrix of a single spheroid over the probability density functions (pdfs) $p(\varphi)$ and $p(\tau)$ that describe the orientation distribution of the scatterers in the volume [29], [27]

$$C_{Vol\,mn} = F_{ir} \iint_{\varphi,\tau} S_m^P S_n^{P*} \cos\tau p\left(\tau\right) p\left(\varphi\right) d\tau d\varphi \quad (8)$$

with $m, n \in \{HH, HV, VV, VH\}$ and i,r $\in \{1,2,3\}$. In the simple case of uniform distributions, $p(\varphi)$ and $p(\tau)$ are defined as $p\left(\varphi\right) = 1/(2\Delta\varphi)$ for $\varphi_0 - \Delta\varphi \leq \varphi \leq \varphi_0 + \Delta\varphi$, and $p\left(\tau\right) = 1/(2\Delta\tau)$ for $\tau_0 - \Delta\tau \leq \tau \leq \tau_0 + \Delta\tau$, where $\Delta\tau$ and $\Delta\varphi$ are the widths and τ_0 and φ_0 the mean values of the distributions. The factor F_{ir} is a constant $(1, 2$ or $\sqrt{2})$ required for each element of $[C_{vol}]$. When two or more types of spheroids are present in the volume, the total (volume) covariance matrix is given by the superposition of the contributions from each spheroid type, accounting for their respective orientation and vertical distributions and assuming the contributions to be uncorrelated.

The off-diagonal elements of the volume covariance matrix $[C_{Vol}]$ are in general complex, implying the presence of a phase (-difference) term induced by the dielectric properties and shape of the particles themselves [30]. In a glacier scenario, volume scattering is mostly related to the presence of ice inclusions in the subsurface layers. Assuming the (real part of the) dielectric constant $\varepsilon_{ice} = 3.1$ [31] and using the model proposed in [30], the icy scatterers induce only negligible co-pol phase differences,

mostly lower than 4° for any incidence angle and particle shape, and for the entire range of frequencies of interest for this article.

Finally, the matrix $[P]$ characterizes the propagation through a medium in terms of two orthogonal polarizations (known as eigen-polarisations) and the corresponding wavenumbers. If the propagation medium has an axis of symmetry, the eigen-polarisations are linear, oriented parallel, and orthogonal to it. Assuming (linear) H and V eigen-polarisations, the propagation matrix (in the Lexicographic-basis) becomes

$$[P] = \begin{bmatrix} e^{-i2\kappa_H z/\cos(\theta)} & 0 & 0 \\ 0 & e^{-i(\kappa_H+\kappa_V)z/\cos(\theta)} & 0 \\ 0 & 0 & e^{-i2\kappa_V z/\cos(\theta)} \end{bmatrix} \tag{9}$$

where κ_H and κ_V are the wavenumbers associated to the H and V polarization. κ_H and κ_V are in general complex accounting for the phase shift with respect to the free space propagation (real part) and the attenuation (imaginary part) by the volume. The (complex) wavenumber κ is related to the electromagnetic properties of the propagation medium through the (complex) relative permittivity (e.g., dielectric constant) $\varepsilon(f_0)$ and for nonmagnetic media

$$\kappa_i = 2\pi f_0 \sqrt{\mu_0 \varepsilon_i (f_0)}, \text{with} i \in \{H, V\} \tag{10}$$

where f_0 is the radar (e.g., wave) frequency and μ_0 the free space permeability.

While ice is assumed in the following to be widely isotropic, with $\kappa_H = \kappa_V$ so that $[P]$ reduces to a scalar, this is not the case for firn because of its anisotropic microstructure [32], [33]. According to [26], firn can be considered as a granular nonscattering medium in which sparse scatterers (e.g., ice lenses, layers, etc.) are uniformly distributed. The firn volume itself is described as a homogeneous two-phase mixture of spatially uniformly distributed and equally shaped spheroidal ice grains imbedded in air. The fact that typical grain sizes are on the order of a few mm, much smaller than the wavelength of most conventional radar remote sensing frequencies, turns firn—at these frequencies—into a nonscattering medium. The permittivity components of the mixture, $\varepsilon_{\text{firn},x,y,z}$, in the $(\hat{x}, \hat{y}, \hat{z})$ orthonormal reference system (see Fig. 1) can be written as [24], [26]

$$\varepsilon_{\text{firn},x,y,z} = \varepsilon_{\text{air}} + \mu\varepsilon_{\text{air}} \frac{\varepsilon_{\text{ice}} - \varepsilon_{\text{air}}}{\varepsilon_{\text{air}} + (1-\mu) \ N_{x,y,z} \ (\varepsilon_{\text{ice}} - \varepsilon_{\text{air}})} \tag{11}$$

where ε_{air} and ε_{ice} are the air and ice permittivity, respectively, μ is the ice volume fraction, which is directly linked to the firn density ($\rho_{\text{firn}} = \mu\rho_{\text{ice}}$, with $\rho_{\text{ice}} = 0.917$ g/cm^3) and $N_{x,y,z}$ the depolarization factors, which depend on the shape of the ice grains expressed by the particle anisotropy A_P (or alternatively S_P).

In order to describe the propagation of the H and V polarized waves through the firn layer the permittivity components of (9) are projected onto the $\hat{h}$ and $\hat{v}$ polarizations direction [24]

$$\varepsilon_{\text{firn},H} = \varepsilon_{\text{firn},x} \ , \ \varepsilon_{\text{firn},V} = \varepsilon_{\text{firn},y} \cos^2\vartheta_r + \varepsilon_{\text{firn},z}\sin^2\vartheta_r \tag{12}$$

where $\vartheta_r = \sin^{-1}(\sin\vartheta/\varepsilon_{\text{firn},H,V})$ is the refracted incidence angle according to the Snell's law. The co-pol phase difference measured by the sensor is related to the wavenumber difference

of the H polarized with respect to the V polarized wave in the firn layer. For a firn layer of thickness l, containing (spatially) uniformly-distributed scatterers, the co-pol phase difference is [24]

$$\Phi = \arg\left\{ \int_0^l e^{-2j\frac{2\pi}{\lambda}\sqrt{\varepsilon_{\text{firn},H}}\frac{z}{\cos\vartheta_r}} \left(e^{-2j\frac{2\pi}{\lambda}\sqrt{\varepsilon_{\text{firn},V}}\frac{z}{\cos\vartheta_r}} \right)^* dz \right\}. \tag{13}$$

The integral in (13) equally weighs the phase (and the respective scattering) contributions coming from different depths, as it does not consider the extinction of the radar signal with depth. For this, an additional term is introduced, which accounts for the vertical distribution of the backscattering in the firn. For simplicity, a uniform distribution (i.e., constant extinction coefficient k_e) is considered in the depth range between 0 m (firn upper surface) and the equivalent firn layer thickness (in the case of multiple layers space out by ice layers) sensed by the radar (l). This corresponds to an exponential vertical profile of the backscattering power

$$\sigma(z) = e^{-\frac{2k_e}{\cos\vartheta_r}z} \text{, with } k_e := \cos\vartheta_r/l . \tag{14}$$

It is worth noticing that here the definition of k_e differs from the one traditionally adopted for interferometric models [34]. In this case, the equivalent firn thickness is used instead of the penetration depth since only the depth intervals characterized by the presence of firn and, therefore, contributing to the co-pol phase difference are considered. At this point, the model in (13) can be modified as

$$\Phi = \arg\left(\int_0^l \sigma(z) \ e^{-2j\frac{2\pi}{\lambda}\left(\sqrt{\varepsilon_{\text{firn},H}} - \sqrt{\varepsilon_{\text{firn},V}}\right)\frac{z}{\cos\vartheta_r}} dz \right). \tag{15}$$

The choice of an exponential $\sigma(z)$ keeps the model complexity low. In fact, the number of parameters remains the same as in (13) despite the additional term, that only depends on the refracted incidence angle and the equivalent firn layer thickness. Accordingly, Φ becomes a function of two (known) radar parameters (λ and ϑ) and three (in general unknown) firn layer properties: density (ρ_{firn}), thickness (l), and grain shape (S_P).

The model in (15) can be inverted to retrieve l if *a priori* information of ρ_{firn} and (S_P) is available. However, the characteristic vertical elongation of firn grains [32] can exclusively interpret positive values of Φ. Moreover, it has to be considered that positive co-pol phase differences can also result, for instance, from multiple reflections occurring in the presence of crevasses, and/or shallow layers of metamorphic snow [35].

Interestingly, a similar modeling approach has been proposed to describe the polarimetric signatures of sea ice, accounting for volume scattering from spheroidal brine inclusions, surface scattering from rough ice interfaces and differential propagation related to birefringent layers of snow and ice [36].

A. Two-Component Scenario for Glacier Zones

The models described previously are used to set up tailored scenarios for the individual glacier zones, accounting for the main sources of scattering expected. The attention is focused on the ablation zone, superimposed ice zone, and (lower) percolation zone. However, the flexibility of the model probably allows to cover additional zones, such as the upper percolation and dry

snow zone by adapting the model configuration accordingly. A two-layer scenario is considered for all three zones of interest to describe the superposition of surface and subsurface scattering contributions, based on the understanding gained from the analysis of TomoSAR and Pol-InSAR studies [37], [38]. Assuming that the surface and subsurface contributions are uncorrelated, the covariance matrix describing the total scattering process can be decomposed into the sum of the surface $[C_{sur}]$ and subsurface $[C_{sub}]$ covariance matrices as in (1).

1) Ablation Zone: The scattering scenario in the ablation zone is typically made of the ice surface overlying a volume of solid glacier ice. The dominant scattering contribution is, therefore, expected to be at the surface and is modeled according to (2)–(4c). Scattering within the ice volume is expected to be secondary and related to the possible presence of inclusions (e.g., impurities, small air bubbles, etc.) and changes of density along depth. However, the presence of crevasses induces localized but significant disturbances to the spatial homogeneity within this zone. Typically, they extend some tens of meter in the horizontal and vertical directions, and can have irregular shapes, which makes the scattering interaction complex. Accordingly, crevasses are considered in the following as spatially localized perturbations of the general ablation zone scattering scenario dominated by surface scattering. Finally, the model includes an anisotropic propagation term related to the presence of (nonscattering) dry snow at the ice surface.

2) Superimposed Ice Zone: In the superimposed ice zone, the scattering is also the superposition of a subsurface volume with the overlying ice surface component. However, the ice surface is here in general smoother than in the ablation zone [39] while the volumetric scattering is triggered by the presence of smaller air inclusions (bubbles) [40], typically present in glacier ice as trapped during the formation process of the layers of superimposed ice. Due to the lack of larger scatterers in the subsurface, their scattering contribution is believed to be significant, even at longer wavelengths, despite their size is in the order of some mm to a few cm. This is even more the case at shallow incidence angles, where surface scattering becomes weak [24]. The scattering model for the superimposed ice is, therefore, based on the superposition of a surface and a volume component according to the respective models introduced previously. Also for this zone, an anisotropic propagation component is included to account for the presence of a shallow snowpack at the surface.

3) Percolation Zone: The subsurface scattering in the lower percolation zone occurs on a mixture of ice lenses and pipes embedded in a background of anisotropic firn. The large sized (several tens of cm) icy inclusions dominate the backscattering behavior while possible contributions from the firn grains, whose size is typically up to a few mm, are neglected. Therefore, the model accounts for the sum of two volume components, associated to oblate (lenses) and prolate (pipes) spheroids, respectively, and an anisotropic propagation component related to the presence of firn, according to (15).

III. Polarimetric Descriptors

The modeled scenarios introduced previously can be used to reproduce polarimetric descriptors extracted from the real data

and provide a physical interpretation of the scattering behavior observed over the different glacier zones.

A. Eigen-Based Polarimetric Descriptors

When it comes to the polarimetric interpretation of scattering processes a popular alternative to model-based decompositions are decompositions based on the diagonalization of the covariance matrix $[C]$ that provide scattering descriptors defined by the eigen-vectors and eigen-values of $[C]$ like the scattering entropy H, the scattering anisotropy A, and mean scattering alpha angle α (derived from the representation of $[C]$ in the Pauli basis) [41], [27].

The scattering entropy H is a parameter ($0 \leq H \leq 1$) that expresses the degree of complexity of the scattering process. In terms of the two-component scattering model in (1), low H values ($H < 0.3$, approximately) are typical for dominant surface-like scattering at the ice surface or at refrozen subsurface melt-layers. The level of H is then determined by the surface roughness [28], [24]. In contrast, high H values indicate the presence of a significant volume scattering contribution. However, different shapes and orientation distributions of the scatterers can generate a large range of entropy values (e.g., $H \to 0$ for aligned or spherical particles while $H \to 1$ for randomly oriented particle volumes) [27], [24]. Finally, the combination of surface and volume scattering mechanisms leads to intermediate H levels depending on the relative contributions.

The scattering anisotropy A is a second parameter ($0 \leq A \leq 1$) defined by the eigen-values of $[C]$ and complements the information provided by H [41], [27] as it expresses the relative importance of secondary scattering contributions. By definition, A becomes small when the entropy is high while it becomes more relevant at intermediate H levels [27]. In this sense, A may increase when a surface scattering component is added to a volume. In addition, the scattering anisotropy decreases with increasing surface roughness and with decreasing volume randomness.

The mean scattering angle α ($0° \leq \alpha \leq 90°$) indicates the type of the mean scattering mechanism. Scattering from a slightly rough surface is associated to α values typically in the range between $0°$ and $30°$, mainly governed by the dielectric properties and widely independent of the roughness condition of the surface [28], [24]. In the case of volume scattering, the corresponding α is widely defined by the scatterers' shape, ranging from a few degrees, in the case of disks, to around $45°$ for dipoles [27], [24]. Finally, higher α values ($50° \leq \alpha \leq 90°$) indicate a large phase difference between the *HH* and *VV* channel such as induced by dihedral scattering processes, which might occur at the ice walls of crevasses.

The interpretation of the three descriptors depends of course on the frequency. For instance, the impact of surface roughness increases at shorter wavelengths: a surface with a root mean square height (rms) of a few cm (e.g., 3 cm) behaves smooth (with low H and α but high A values) at L-band (as the wavelength is much larger than the rms height) while it appears rough at *X*-band (with higher H and α but lower A values) where the wavelength is on the order of the rms height.

B. Copolarization Ratio and Phase Difference

As shown in [24], it is convenient to consider two additional polarimetric quantities in order to complement the information provided by the eigen-based descriptors: the *copolarization* (co-pol) *power ratio* P, and the *co-pol phase difference* Φ.

The co-pol ratio is here defined as

$$P = \langle |S_{HH}|^2 \rangle / \langle |S_{VV}|^2 \rangle \qquad (16)$$

and can provide information about the mean orientation of the scatterers in a volume or the roughness condition of a scattering surface [28], [24].

The co-pol phase difference, here defined as

$$\Phi = \arg \left(\langle S_{HH} S_{VV}^* \rangle \right) \qquad (17)$$

can be used to complement the information provided by α concerning the presence of dihedral scattering or differential propagation in dielectrically anisotropic (birefringent) media, like firn and snow. Finally, nonzero values of Φ can result from volumes of scatterers if the latter possess a preferred orientation. In this case, differential propagation occurs similar to the case of birefringent media, depending on the shape and dielectric properties of the scattering particles. The information carried by the co-pol phase difference is, up to some extent, similar to the α angle: a large (positive or negative) Φ are associated to a large α and vice versa. However, Φ offers a more direct link to dielectric properties of the scatterers. The anisotropic propagation model described previously represents an example of how co-pol phase differences can be related to firn properties.

IV. TEST SITE AND EXPERIMENTAL DATA

The study area is the K-Transect, starting approximately 20 km east of Kangerlussuaq (67°00' N, 50°41' W), at the southwestern margin of Greenland, and running eastward towards the inner part of the ice sheet, roughly parallel to the 67°N latitude circle. In the frame of the ARCTIC15 experiment, fully polarimetric SAR data at X-, C-, and L-band were simultaneously acquired on 21 May 2015 by DLR's F-SAR airborne system over a 200 km long (and approximately 5 km wide) transect. The "ascending" swath starts at the ice margin and crosses the ablation and SI zone, in W-E direction, up to the percolation zone (approximately 2100 m a.s.l.), while the "descending" swath has the opposite heading.

The (single-look complex SLC) data in all frequencies have been acquired with a spatial resolution of 2.0 m in (slant-) range and 0.5 m in azimuth. The incidence angle varies across the swath from 25° (in near-range) to 65° (in far-range). During the whole campaign, the air temperature was steadily below 0°C, so that dry snow and ice conditions were preserved.

As reported in [42], the surface mass balance at the K-transect suffered from an accelerating negative trend between 2010 and 2014 with a consequent increase of the equilibrium line altitude from around 1550 m a.s.l. (long term EL) to around 1730 m a.s.l. [43]. Shallow ice cores and ground-penetrating radar measurements conducted in spring 2013 indicated that no firn was present below 1680 m a.s.l., fixing the FL at this altitude (FL2013) [42]. The same study reports the presence of a 5 m thick ice layer in the

shallow subsurface at 1850 m. However, the trend decelerated in 2015 when the EL was located slightly above 1500 m a.s.l. [44], at similar altitude as in the period 1990–2010.

The ablation zone roughly extends from the coast up to the long-term EL. The lack of information about the FL location in 2014 allows only an approximate location of the SI zone, which is here assumed to extend from the upper boundary of the ablation zone up to the FL2013 (1680 m a.s.l.). The negative mass balance trend suggests that the FL might have migrated further upward in 2014. Finally, the percolation zone is located above the FL2013 (see also Fig. 3). The area between the FL2013 and the EL2014 (located at 1730 m a.s.l.) is considered to be part of the transition from SI to the percolation zone, where the subsurface consists of a mixture of firn and ice layers.

Fig. 2 shows a Pauli RGB representation of the two headings at L-band superimposed to an optical image of the area, as well as the location of the FL2013 (red line), the EL2014 (grey), and the long term EL (white). The change of polarimetric behavior in the different glacier zones is evident: the percolation zone is dominated by greenish colors, indicating the presence of strong volume scattering whereas the ablation zone is mostly bluish, apparently dominated by surface scattering.

V. RESULTS AND DISCUSSION

A. Polarimetric Analysis

The polarimetric analysis in this section shall assess the potential of the proposed descriptors to map the different glacier zones at the different frequencies. For each frequency, the 4X4 covariance matrices are formed using an estimation window with ∼150 independent samples, corresponding to a 30X30 m window on ground. By performing additive noise compensation according to [45], the covariance matrices are reduced to the conventional 3X3 form. After this, the polarimetric entropy, anisotropy and mean alpha angle as well as the co-pol ratio and the co-pol phase difference are estimated. Figs. 3–5 depict the five PolSAR descriptors for the "ascending" swath at X-, C-, and L-band, respectively. In order to facilitate the interpretation, the elevation profile of the study area as well as the location of the FL2013, the EL2014 and the long term EL are shown in the top panel of Fig. 3. By comparing the three figures, a number of features common to all frequencies become obvious, such as a refrozen supraglacial lake at 105 km distance as well as crevasses (e.g., between 40 and 75 km distance) and melt channels in the ablation zone. Their presence can lead to significant deviations from the expected ablation zone scattering scenario as sketched in Fig. 3. In contrast, most of the PolSAR parameters exhibit a smooth spatial behavior over the percolation zone, confirming the expectation of a homogeneous scattering scenario, as depicted in Fig. 3.

For the multifrequency comparison, the frequency-dependent penetration of the SAR signal into the glacier subsurface has to be considered. Tomographic data acquired in the frame of the same campaign along the EGIG line (about 350 km north of the K-Transect), which is classified as lower percolation zone like the uppermost portion of the transect under study, reported the presence of significant scattering sources down to a depth
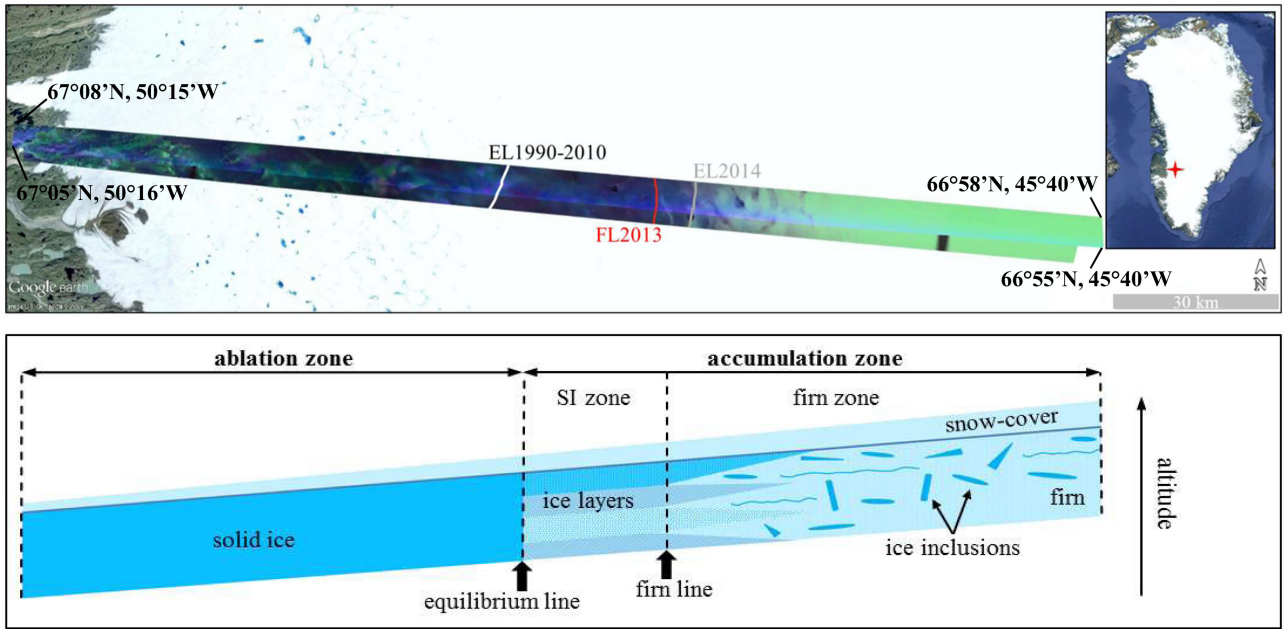
Fig. 2. Upper panel - Pauli RGB representation of the L-band SAR headings overlying an optical image of the K-transect, in south-west Greenland. Red: *HH-VV*, Green: *HV+VH*, Blue: *HH+VV*. The red line indicates the FL 2013 (1680 m a.s.l.), while the long term EL and the EL 2014 are represented by the white and grey line, respectively. The corners' coordinates of the "ascending" heading are reported as geographic reference. The inset shows the location of the study area with respect to the entire ice sheet. Lower panel – Sketch of the subsurface structure of the glacier zones existing in the study area.
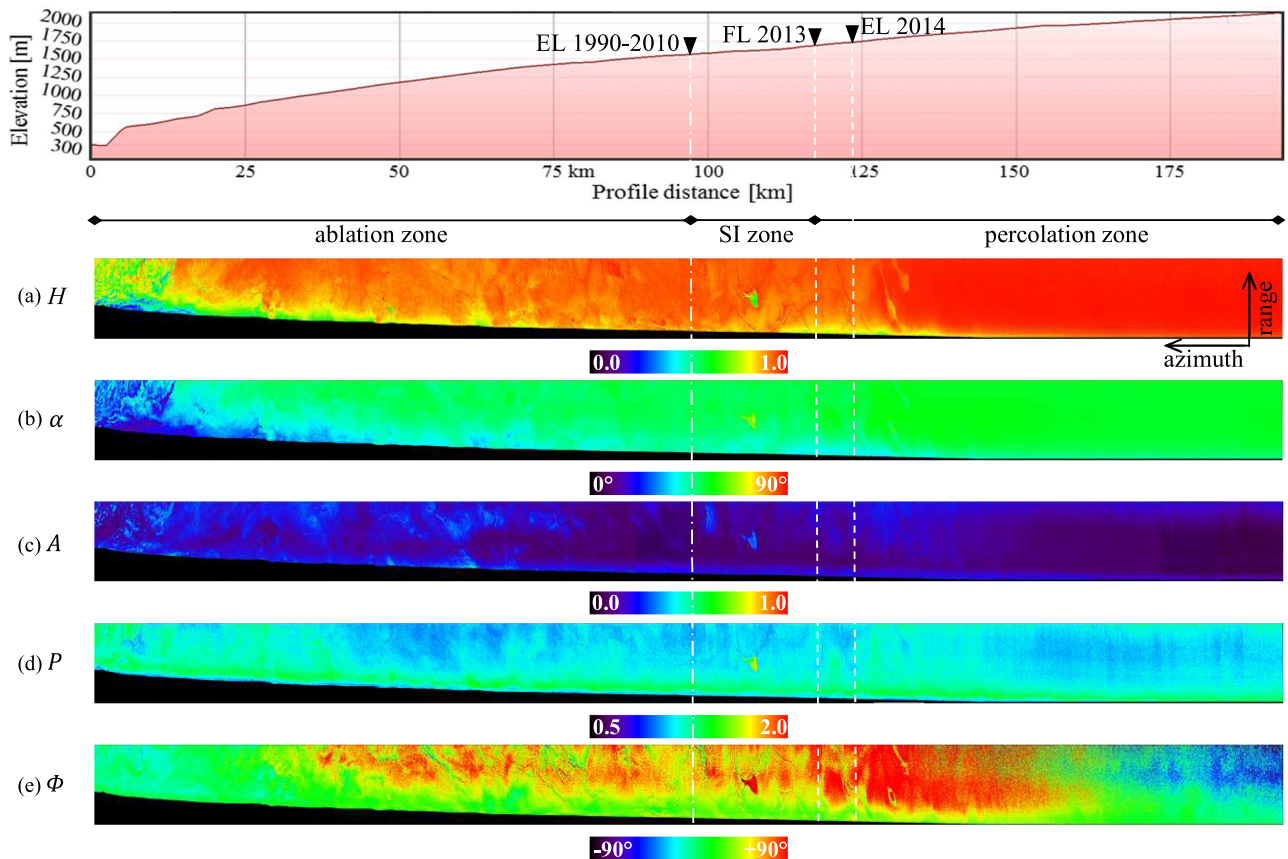

Fig. 3. Top panel – Elevation profile of the study area and corresponding location of the FL2013, the long term EL and the EL2014; (a)—(e) Polarimetric descriptors extracted from X-band SAR data (E-W heading).
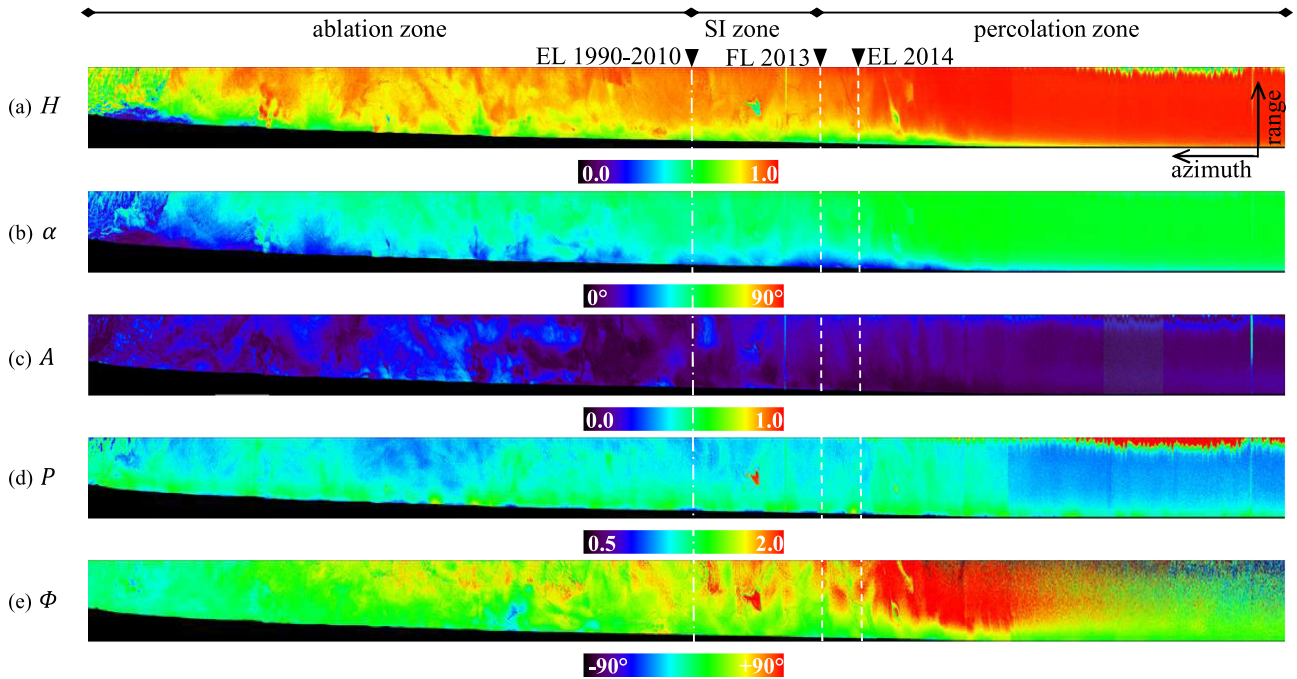
Fig. 4.   Polarimetric descriptors extracted from the C-band SAR data (E-W heading) and corresponding location of the FL2013, the long term EL and the EL2014.
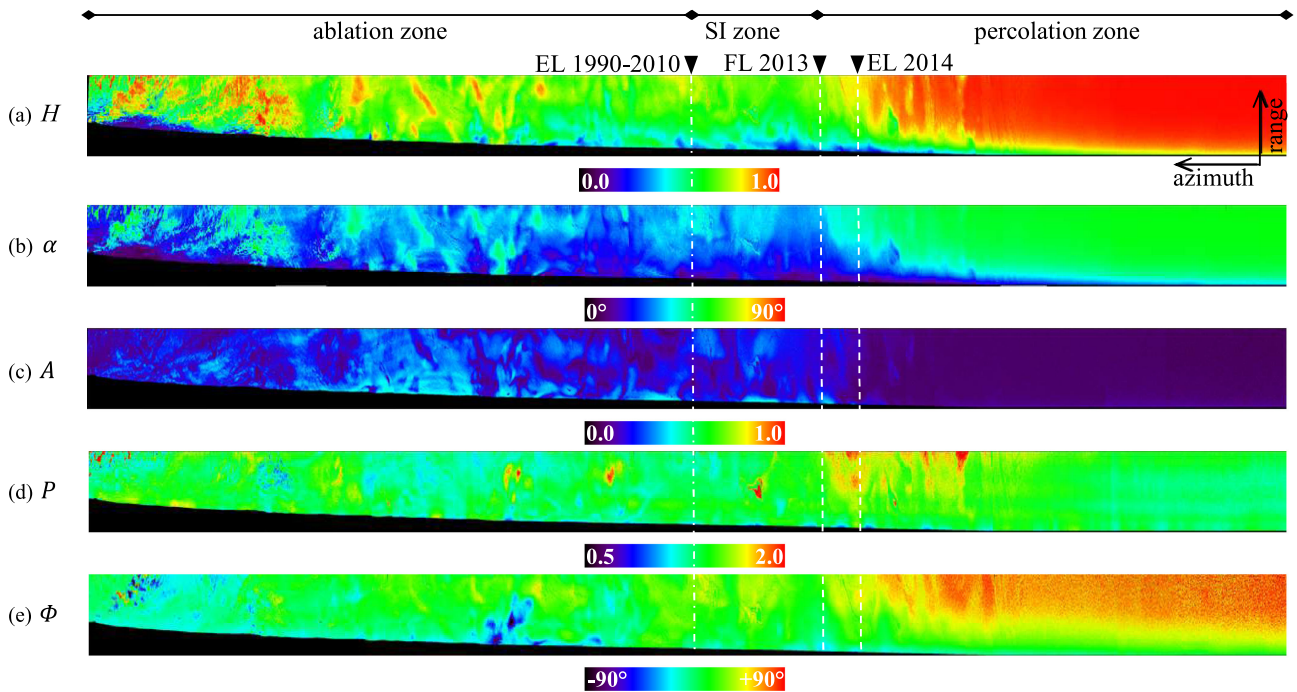
Fig. 5.   Polarimetric descriptors extracted from the L-band SAR data (E-W heading) and corresponding location of the FL2013, the long term EL and the EL2014.
.

of 6–10 m at both X- and C-band, and of 15–20 m at L-band [37]. A second ARCTIC15 tomographic dataset acquired in the ablation zone of the K-Transect (at approximately 500 m a.s.l.) revealed scattering contributions limited to a depth range of 3–5 m at X-band, 10–15 m at C-band, and 50–60 m at L-band [38]. The results make clear that, in general, one has to account for surface and subsurface contributions in all zones and frequencies justifying the use of a 2-layer model for the interpretation of the data.

To support the analysis, azimuth profiles of the five polarimetric descriptors along the whole transect, averaged over 500 range samples at mid-range (associated to an incidence angle of about 50°), are plotted in Fig. 6 and discussed in the following.
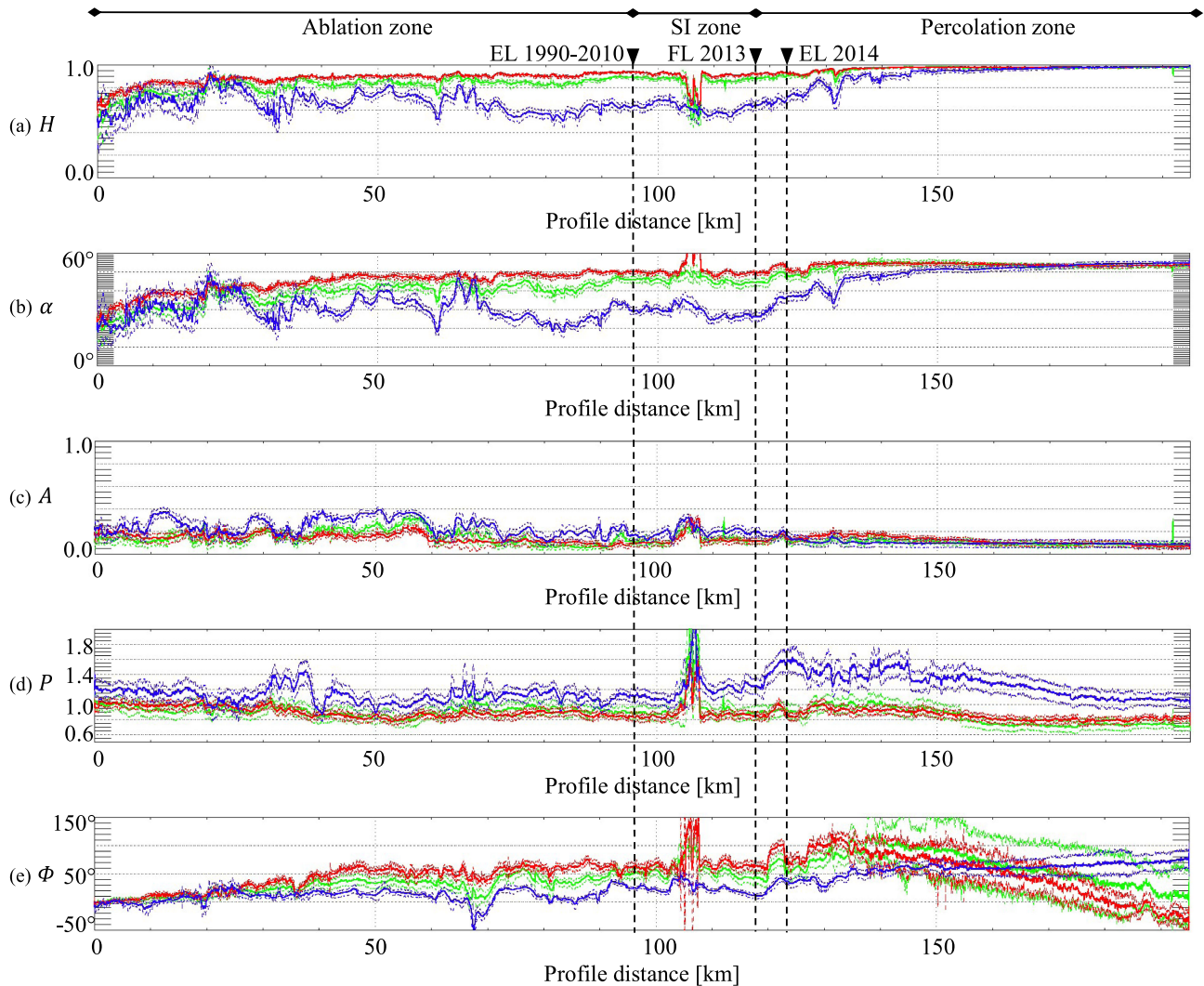
Fig. 6. Azimuth profiles and standard deviations (dashed lines) of the PolSAR signatures extracted at mid-range, with an average incidence angle of 50°, for the three available frequencies (Red: X-band, Green: C-band, Blue: L-band). The black dashed lines indicate the location of the FL2013 and the long term EL.

1) Interpretation of the X-Band PolSAR Signatures: The X-band entropy map in Fig. 3(a) shows overall high values across the whole K-transect with a gradual increase from 0.80 to almost 1 when moving from lower to higher elevation [see also Fig. 6(a)]. The very high (almost 1) and stable values over the percolation zone, between 130 km distance (1800 m a.s.l.) and the end of the transect, indicate the presence of a dominant high entropy volume scattering component originating from ice inclusions in the firn layer. At around 130 km distance, entropy decreases from 0.99 to 0.9, just above the EL2014. Here, at the transition between firn and the superimposed ice zone, thick ice layers gradually replace firn in the glacier subsurface and it is reasonable to expect the presence of a surface-like scattering component that reduces the overall entropy. At lower elevations, in the ablation zone, H has values mostly between 0.85 and 0.9 with local variations associated to the presence of crevasses and other surface melt-features. Here, the overall values might appear very high for a scenario where scattering from the ice surface is expected to be the dominant contribution. However, given the short wavelength (3 cm), already a moderate roughness

(rms surface height of some cm) causes significant depolarization, which results, in turn, in high entropy values [46]. The overall high entropy leads to very low anisotropy values (0.1-0.2) along the whole transect, as shown in Figs. 3(c) and 6(c), limiting its sensitivity to the different zones. This is reflected by the mean α angle map in Fig 3(b) as well. The corresponding profile in Fig. 6(b) shows values increasing with elevation from around 30° to 50° over the lower part of the ablation zone, in the first 45 km of the transect. From here, α remains stable around 50° up to the location of the EL2014, close to the boundary between the SI and percolation zone, where a small increase to 55° is observed. This supports the interpretation of the entropy concerning the dominant scattering mechanisms.

The interpretation of the three eigen descriptors is complemented by the co-pol power ratio and phase difference. The co-pol power ratio map, shown in Fig. 3(d), and the corresponding azimuth profile in Fig. 6(d) show values mainly within the range 0.8-1.1, without any significant trend with elevation and no sensitivity to the different zones. In particular, such behavior might result from the fact that both a rough surface (in the

ablation zone) and a volume of randomly oriented scatterers (in the percolation zone) exhibit similar *HH* and *VV* backscattered powers.

Finally, the co-pol phase difference map in Fig. 3(e) indicates mainly positive values, except for a few confined areas in the ablation zone and the upper part of the percolation zone. Φ values are characterized by an overall increase from about 0° at the ice margin up to around 100° at 130 km distance [see also Fig. 6(e)], slightly above the EL2014. Moving to higher altitude, Φ slowly decreases reaching negative values (around −40°). A smooth spatial behavior is observed in the percolation zone, similar to the other parameters, while a more irregular pattern is observed over the ablation and SI zones, reflecting the spatial distribution of crevasses and surface roughness. The large positive values, up to 100°, observed in Fig. 6.3 between 120 km and 150 km distance, are attributed to propagation through the firn present above the FL2013. The decrease of Φ observed at higher elevation could be instead related to a gradual increase of fresh snow with altitude, as suggested by the accumulation gradient measured along the transect [47]. In fact, the typical horizontal orientation of ice grains in fresh snow (contrarily to firn) generates a negative *HH-VV* phase difference contribution [35] that can overcompensate the positive values due to the underlying firn layer, if enough fresh snow is present at the surface.

The analysis of the descending swath leads to very similar results.

Summarizing, X-band PolSAR measurements are only of limited use for glacier zones mapping. The main information is obtained from the spatial behavior of the analyzed descriptors at different altitudes. It is very homogeneous in the percolation zone and becomes more heterogeneous at lower elevations due to the increasing surface roughness and the appearance of localized features in the SI and ablation zones. A unique potential of X-band, compared to longer wavelengths, is given by the sensitivity in terms of co-pol phase difference to the shallow snow-cover, which is more difficult to detect using C- and L-band measurements due to their increased sensitivity to the subsurface firn layers.

2) Interpretation of the C-Band PolSAR Signatures: The C-band descriptors behave very similar to the ones at X-band. Slightly lower entropy and mean alpha angle [see Fig. 6(a) and (b)] values as well as a more pronounced variation of both parameters with the incidence angle in the ablation zone [see Fig. 4(a) and (b)] are observed at C-band. This can be interpreted by the decreasing roughness conditions due to the longer wavelength. In contrast, the strong volume scattering contribution in the percolation zone is confirmed by H and α values, similar to the X-band case. Consequently, the anisotropy remains fairly low throughout the whole transect.

While no significant difference in the co-pol ratio shown in Fig. 6(d) is observed when compared to X-band, an overall decrease of the co-pol phase difference (around 20° at mid-range compared to X-band) can be observed, especially below 1800 m elevation [130 km distance, see Figs. 4(e) and 6(e)]. In particular, Φ decreases significantly in the elevation range between 1800 m a.s.l. and the FL2013 location. The reduced impact of surface roughness allows an interpretation since a smoother surface is

less prone to generate co-pol phase differences. At higher altitudes, a decreasing trend of Φ similar to X-band is observed. As in the previous case, the increase of fresh snow in the uppermost portion of the transect can interpret such behavior. However, it is interesting to notice that the C-band trend is less pronounced since the longer wavelength ensures higher sensitivity to the underlying firn layer compared to X-band.

In conclusion, C-band polarimetric measurements show a slightly higher sensitivity to the glacier zones than X-band primarily due to the reduced impact of surface roughness. The co-pol phase difference allows a sensitive detection of the percolation zone boundary but is also less sensitive to the presence of fresh snow at the surface.

3) Interpretation of the L-Band PolSAR Signatures: The polarimetric descriptors at L-band shown in Fig. 5 are substantially different from the corresponding ones at X- and C-band. H and α [see Fig. 5(a) and (b)] are significantly lower in the SI and upper ablation zone, fluctuating around 0.6 and 20°-35° [see also Fig. 6(a) and (b)], respectively indicating the occurrence of a strong surface scattering component (at the ice surface). In the ablation zone, higher H and α values are observed over the main crevasse fields. In these cases, the L-band behaves similarly to the higher frequencies as such features are typically large enough to produce complex interactions with the radar signal even at longer wavelengths. In the percolation zone, starting at 145 km distance [see Fig. 6(a) and (b)], H and α have similar values at all frequencies, constantly above 0.9 and 50°, respectively. This indicates that volume scattering from ice inclusions in the firn is the dominant contribution at L-band as well. The steep decrease observed for both parameters in the area of the EL2014 and FL2013, between 130 and 115 km distance, fits well with the expected decrease of the firn layer thickness and the associated reduction of embedded scatterers, in favor of an increasing surface-like scattering contribution from subsurface ice layers.

Interestingly, the pronounced variation of the L-band entropy across the zones is only partially reflected in the behavior of the anisotropy [see Fig. 5(c)]. Extremely low values are observed over the percolation zone, similarly to the X- and C-band case. In contrast, a slight increase can be noticed in the SI zone [see also Fig. 6(c)], whit values fluctuating between 0.1 and 0.3. Finally, A values increase up to 0.4 in the ablation zone, revealing the presence of a significant secondary scattering contribution in addition to the dominant surface scattering, likely from crevasses.

The co-pol ratio does not show significant variations across the glacier zones [Fig. 5(d)], similarly to the C- and X-band case. However, overall higher values are found at L-band, especially over the percolation zone [see Fig. 6(d)]. Here, values range between 1.0 and 1.6, pointing out the presence of horizontally oriented scatterers, such as ice lenses. Also here, a steep decrease, from 1.6 to around 1.2 is observed between the EL2014 and FL2013, fitting well with the expected decrease of volume scattering from the oriented inclusions in favor of an increase of surface scattering from subsurface (superimposed) ice layers.

The co-pol phase difference shows a slight gradual decrease from the uppermost area of the transect down to 1850 m a.s.l., as shown in Figs. 5(e) and 6(e). From here to approximately 1700 m

TABLE I
TWO-COMPONENT MODEL CONFIGURATION FOR THE SCATTERING SCENARIO
IN THE ABLATION ZONE

X-Bragg Surface component		
s [cm]	ε_{snow}	ε_{ice}
3.0	1.5	3.1-j0.0004
Volume component (prolates)				

S_p	τ_0 [deg]	$\Delta\tau$ [deg]	φ_0 [deg]	$\Delta\varphi$ [deg]
10	0	35	0	180

TABLE II
TWO-COMPONENT MODEL CONFIGURATION FOR THE SCATTERING SCENARIO
IN THE SI ZONE

X-Bragg Surface component		
s [cm]	ε_{snow}	ε_{ice}
1.0	1.5	3.1-j0.0004
Volume component (prolates)				

S_p	τ_0 [deg]	$\Delta\tau$ [deg]	φ_0 [deg]	$\Delta\varphi$ [deg]
10	0	35	0	180

TABLE III
TWO-COMPONENT VOLUME MODEL CONFIGURATION FOR THE SCATTERING
SCENARIO IN THE PERCOLATION ZONE

Oblates volume component				
S_p	τ_0 [deg]	$\Delta\tau$ [deg]	φ_0 [deg]	$\Delta\varphi$ [deg]
0.5	90	15	0	180
Prolates volume component				
S_p	τ_0 [deg]	$\Delta\tau$ [deg]	φ_0 [deg]	$\Delta\varphi$ [deg]
10	90	90	0	180

elevation, a remarkable decrease is observed with values as low as 20° at the FL2013 [see also Fig. 6(e)], where the amount of firn decreases continuously until it completely disappears [42]. Below 1700 m, Φ values gradually approach 0°, indicating the complete absence of firn. However, co-pol phase differences up to 20° appear often below the FL2013 probably caused by the presence of some tens of cm of metamorphic snow [26] at the ice surface. Localized areas with larger (either positive or negative) deviations are associated to the complex scattering (including even reflections) from crevasses (e.g., between 40 and 70 km distance).

When comparing the three frequencies, L-band descriptors provide a clearer identification of the different glacier zones due to the deeper penetration and the lower sensitivity to surface roughness. In particular, the percolation zone can be identified in all five polarimetric descriptors due to the distinctive change of the scattering process at the FL location. The co-pol phase difference allows furthermore an accurate characterization of the percolation zone boundary, offering also the potential for model-based inversion of firn properties. In contrast, the separation of the ablation and SI zones and, therefore, the identification of the long term EL is more difficult.

4) Range Profiles Modeling: So far, the suitability of the proposed model to describe the polarimetric data in the different zones has been discussed only in qualitative terms. For a more quantitative evaluation, the incidence angle dependency of the selected polarimetric descriptors predicted by the model is compared to the ones observed in the experimental data. For this, representative range profiles of the five polarimetric descriptors in the three different zones, extracted over homogeneous areas (around 1000 m a.s.l. in the ablation zone, 1650 m a.s.l. in the SI zone, and 2000 m a.s.l. in the percolation zone) and averaged over 10000 azimuth lines, corresponding to a spatial extend in azimuth of about 2 km, are used and shown in Fig. 7. The ability of the two-component surface and volume scattering model to interpret the (range dependent) behavior of the polarimetric descriptors in the three zones is assessed and discussed in the following while the model configurations employed for the single glacier zones are summarized in Tables I– III.

a) Ablation zone

In the ablation zone (see Fig. 7, left column), a clear increase of entropy with increasing incidence angle at X- (red line) and C-band (green line), from 0.6 to 0.9 and from 0.5 to 0.85, respectively, is observed. The L-band values (blue line) rise more smoothly, from 0.45 to 0.6. A similar behavior is observed for the mean alpha angle, increasing from 30° to 50° at X-band,

from 20° to 45° at C-band, and from 15° to 30° at L-band. In general, such values can be explained with the superposition of a dominant slightly rough surface and a secondary subsurface volume component. The surface contribution decreases with increasing incidence angle [27], while the volume component remains constant. The decrease of the surface-to-volume ratio makes the entropy and alpha angle values to rise in far range where the volume component becomes more significant. Such behavior can be reproduced by the model configuration defined in Table I simulating the superposition of a scattering component from a slightly rough snow/ice interface and a contribution from a volume of prolates accounting for the possible presence of air bubbles in the ice. The dielectric discontinuity at the snow/ice is defined by assuming a snow permittivity $\varepsilon_{snow} = 1.5$, corresponding to a typical density of $\rho = 0.25$ g/cm^3 [48], since no reference data is available. Finally, surface roughness is selected to be the maximum allowed by the X-Bragg model w.r.t the L-band wavelength since the ice surface is expected to be rather rough in the ablation zone. For the volume component, an arbitrary value of S_p is selected to account for elongated bubbles [40] or other scattering inclusions, since no reference information is available. According to the employed model, a partial horizontal orientation of the prolates represents the only possible interpretation for the L-band co-pol ratio values larger than 1, since the X-Bragg surface component predicts values ≤ 1 in any case. Nevertheless, this interpretation seems to disagree with observations reporting a preferred vertical elongation of air bubbles in ice layers [40]. One possible reason might lie in the low sensitivity of the longer L-band wavelength to such small scatterers. This interpretation is supported by the fact that both C- and L-band co-pol ratios mostly assume values < 1, suggesting higher sensitivity to vertically oriented scatterers (see Fig. 7). The fitting between data and model is then achieved by using the surface-to-volume intensity ratio as a free model parameter.
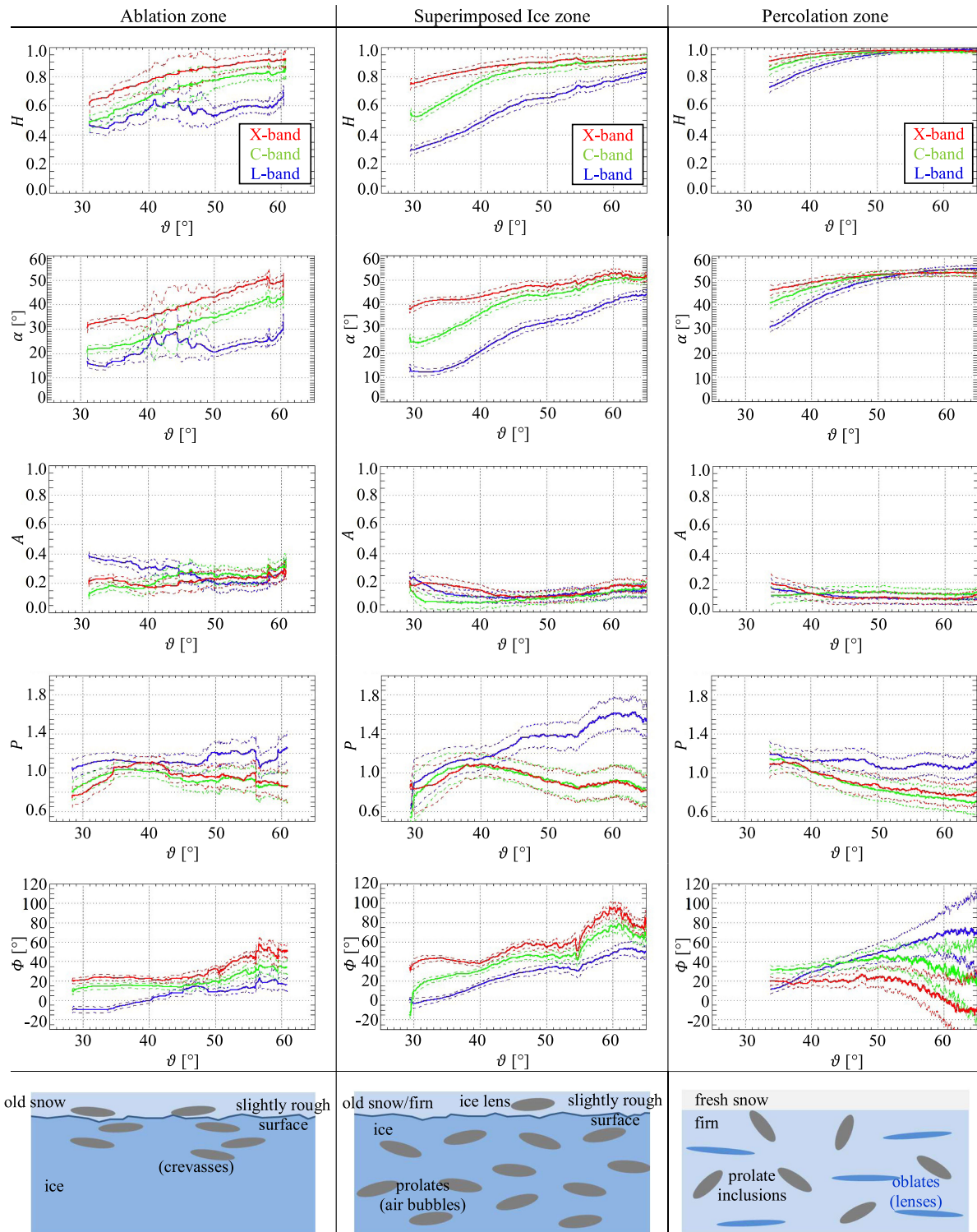
Fig. 7. From left to right, range profiles (solid lines) and standard deviations (dashed) of the PolSAR descriptors in the ablation zone (at around 1000 m a.s.l.), superimposed ice zone (∼1650 m a.s.l.), and percolation zone (∼2000 m a.s.l.). Red: X-band, Green: C-band, Blue: L-band. Bottom panels: sketch of the simulated scattering scenarios for the three different zones.

At L-band, the range profiles of H, α, A, and P can be interpreted satisfactorily by surface-to-volume ratios fluctuating between 5.0 and 2.0 along range. The same scenario results in a general decrease of the surface-to-volume ratio at higher frequencies, ranging from around 3.0 to 1.0 at C-band, and

from 1.5 to around 0.01 at X-band with increasing incidence angle. In contrast to the reduced penetration, which leads to an increase of the surface contribution, the two higher frequencies are more affected by roughness induced depolarization, which is misinterpreted as a volume component. Also, the employed

surface model (X-Bragg) is only valid for slightly rough surfaces interpreting best the L-band data. As the same surface appears rougher at higher frequencies, the model cannot describe properly the C- and X-band data. Finally, the observed Φ profiles are in accordance at all frequencies with the increasing differential propagation effects with the incidence angle through a shallow layer of metamorphic snow at the glacier surface.

b) Superimposed-ice zone

In the SI zone (see Fig. 7, mid column), the C- and L-band profiles of H and α show a steeper increase with the incidence angle (H from 0.55 to 0.9 and α from 25° to 50° at C-band, H from 0.3 to 0.8 and α from 12° to 43° at L-band from near to far range) than in the ablation zone, while a more stable and overall higher values are observed at X-band (H from 0.75 to 0.9, α from 38° to 50°). Interestingly, the two lower frequencies show a larger variation in the near range, between 30° and 45° incidence angle. As already discussed for the ablation zone, this behavior suggests the presence of a strong surface scattering component in the near range, and a gradually increasing volume component in far range. In contrast, the X-band values show a smaller variation across range which is likely due to the increased effect of roughness. The model configuration for the superimposed zone is the same as for the ablation zone, with the only exception represented by a reduced surface roughness [39].

The L-band behavior can be reproduced by the two-component model in terms of a smooth surface and a volume of oblate spheroids with a preferred horizontal orientation (see Table II) for surface-to-volume ratios ranging from approximately 10 in the near range to around 1.0 in the far range. Compared to the values obtained for the ablation zone, remarkably stronger surface scattering component is found, especially at steep incidence angles. This can be attributed to the generally smoother ice surface in the SI zone [39]. On the other hand, the presence of an oriented volume component can be interpreted by the presence of (a few) ice lenses embedded in patches of remaining firn or to bubbly ice layers [40].

Moving to C- and X-band, the same model configuration predicts lower surface-to-volume ratios (from 2.5 to 0.05 at C-band and from around 1.0 to less than 0.05 at X-band) as a consequence of the increased roughness effect and the insufficiency of the X-Bragg model to correctly describe this roughness range.

Finally, Φ shows positive and gradually increasing values with the incidence angle at all frequencies. This can be explained by the anisotropic propagation model in Section III with the increase of standing metamorphic snow in this elevation range.

c) Percolation zone

In the percolation zone (see Fig. 7, right column), the scattering complexity increases significantly at L- and C-band, reaching the same levels of H and α as at X-band. The volume scattering contribution becomes dominant in all frequencies. Accordingly, the profiles at the three frequencies become very similar to each other for all descriptors. However, the increasing range trend observed especially at L-band reveals the presence of a weak preferred orientation of the scatterers [24]. This is also supported by the co-pol ratio profiles which deviate now from the unit. However, while the X- and C-band co-pol ratio

values are in general smaller than 1, indicating a vertical orientation, the L-band profile indicates values slightly larger than 1, pointing out a (weak) horizontal orientation of the scatterers. This difference can be explained by assuming different sets of scattering particles at the different wavelengths, depending on their size. For instance, small ice clusters in shallow subsurface layers can provide significant backscattering at X-band while they remain insignificant at L-band. Also, large ice inclusions (e.g., lenses), with dimensions on the order of some tens of cm, can act as volume particles at L-band and appear as surface-like scatterers at C- and X-band.

The behavior of the data can be reconstructed by a volume scattering component generated by a mixture of two particles types: oblates, acting as ice lenses, and prolates representing all other inclusion types (pipes, clusters, etc.). The configuration used to interpret the data is defined by the values in Table III. The volume model is complemented by the anisotropic propagation component to account for the presence of firn (as well as fresh snow in the C- and X-band case). Arbitrary values of S_p have been chosen for oblates and prolates in order to simulate an exemplary case. The canting angle distributions (φ_0 and $\Delta\varphi$) describe oriented clouds of scatterers for both oblates and prolates since neither lenses nor pipes are expected to have a preferred orientation in the horizontal plane. The tilt angle distribution (τ_0 and $\Delta\tau$) of the oblates accounts for a cloud of widely horizontal lenses, in agreement with available literature [22]. Less straightforward is the interpretation of tilt angle distribution of prolates, which provides the best match between simulated and real PolSAR signatures when it defines randomly oriented scatterers. This seems to be in contrast with the expected vertical orientation of pipes [22]. One possible explanation is that this scattering component includes a significant contribution from scatterers other than pipes, e.g., ice layers and glands having more complex shapes than prolates [1], and which are not included in the employed model.

The model matches the observed profiles at L-band for a prolates-to-oblates power ratio ranging from 0.2 in near range to approximately 1.5 in far range. That is, the relative contribution from ice lenses is expected to decrease significantly with the incidence angle, due to their horizontal alignment [24]. Moving to C- and X-band, the model indicates a significant increase of the contribution from random prolates, with values of the prolates-to-oblates ratio ranging from 1.0 to 5.0 at C-band and 1.5 to 5.0 at X-band. Such result confirms the indication of a change in the scattering scenario across frequency due to the fact that smaller and randomly oriented particles might become effective scatterers at shorter wavelengths.

Concerning the observed Φ profile, the small positive values observed at near range in X-band and C-band confirm the limited penetration and the sensitivity only to a shallow firn layer [37]. The decrease observed in far range, from around 20° to –15°, supports the hypothesis of a layer of fresh snow present at the surface generating a negative contribution to the measured Φ. At L-band, the deeper penetration allows to sense a thicker firn layer, that causes the observed positive and gradually increasing Φ with range.

VI. CONCLUSION

The potential of model-based interpretation of polarimetric SAR data for the characterization of glacier zones in west Greenland has been investigated at different frequencies. For this, a generic two-component model that describes surface and subsurface scattering contributions in the different glacier zones has been established. The (anisotropic) propagation through snow, firn and ice layers is also accounted as it plays an important role in the interpretation of the observed polarimetric signatures.

A set of five polarimetric descriptors consisting of the scattering entropy, the mean scattering alpha angle, the scattering anisotropy, the co-pol power ratio and the co-pol phase difference has been used to describe the projection of the model on the scattering of each zone. For the analysis, a multifrequency (X-, C-, and L-band) airborne dataset acquired over the K-transect, covering a 200 km long swath across the ablation, superimposed ice and lower percolation zone of the ice sheet has been used.

The potential to differentiate the glacier zones from each other increases with decreasing frequency due to the decreasing impact of surface roughness and the increasing penetration into the ice subsurface. In this sense, it is at L-band where the transition from the percolation zone to the superimposed ice zone (e.g., the firn line) becomes clearly visible in all PolSAR descriptors. The transition between the superimposed ice zone and the ablation is, however, more difficult to detect. At C- and X-band, surface roughness makes the polarimetric signatures more uniform across the zones. Nevertheless, the higher frequencies allow to sense (shallow) layers of fresh snow that are almost transparent at L-band by means of the co-pol phase difference.

A full validation of the proposed approach is, however, hampered by the lack of reference data regarding the shape and orientation of the scattering inclusions as well as of the ice surface roughness in the different zones. Some limitations arise then from the assumptions, which the different model components are built on. First, the employed surface component (X-Bragg) is insufficient to describe polarimetric scattering at (very) rough surfaces, as it is the case of the ablation zone especially for the higher frequencies. Second, the dielectric properties of snow, ice, and firn (i.e., permittivity, density, anisotropy, etc.) are assumed spatially homogeneous and constant with depth. Third, each class of scattering inclusions (i.e., ice lenses, pipes, and air bubbles) is assumed to be composed of equally shaped and distributed objects. A further simplification is made by neglecting possible scattering contributions originated by multiple interactions and multiple ice layers in the firn of the percolation zone.

Nevertheless, the use of a generalized scattering model, as the one proposed here, allows to characterize the main scattering mechanisms in each glacier zone, providing a clear link to the respective subsurface structure. In addition, the propagation component of the model establishes a link between the physical properties of firn, providing a potential tool to access information relevant for the estimation of surface mass balance. The results indicate also the potential of combining multifrequency polarimetric observations to exploit their complementarity in terms of sensitivity to different surface and subsurface scattering structures.

The modeling of additional PolSAR observables, like backscattering coefficients, should be addressed in the future, which might allow the retrieval of scatterers' number and size. Such information would be useful to quantify the amount of refrozen meltwater retained in the snow and firn layers.

Finally, the proposed model has the advantage of being easily transferable to the space-borne case to be tested for glacier zones' mapping on larger scale. Of particular interest will be its application to the next multifrequency generation of satellite SAR missions with fully polarimetric capabilities.

REFERENCES

[1] W.S.B. Paterson, *The Physics of Glaciers*, 3rd ed. Oxford, U.K.: Pergamon, 1994.

[2] I. Joughin, D. P. Winebrenner, M. Fahnestock, R. Kwok, and W. Krabill, "Measurement of ice-sheet topography using satellite-radar interferometry, " *J. Glaciol.,* vol. 42, no. 140, pp. 10–22, Jan. 1996.

[3] M. Rankl and M. Braun, "Glacier elevation and mass changes over the central Karakoram region estimated from TanDEM-X and SRTM/X-SAR digital elevation models," *Ann. Glaciology*, vol. 57, no. 71, pp. 273–281, 2016.

[4] I. R. Joughin, D. P. Winebrenner, and M. A. Fahnestock, "Observations of ice-sheet motion in Greenland using satellite radar interferometry," *Geophys. Res. Lett.*, vol. 22, no. 5, pp. 571–574, Mar. 1995.

[5] E. Rignot, K. C. Jezek, and H. G. Sohn, "Ice flow dynamics of the Greenland ice sheet from SAR interferometry," *Geophys. Res. Lett.*, vol. 22, no. 5, pp. 575–578, Mar. 1995.

[6] R. Kwok and M. A. Fahnestock, "Ice sheet motion and topography from radar interferometry," *IEEE Trans. Geosci. Remote Sens.*, vol. 34, no. 1, pp. 189–200, Jan. 1996.

[7] E. Rignot, S. P. Gogineni, W. B. Krabill, and S. Ekholm, "North and northeast Greenland ice discharge from satellite radar interferometry," *Science*, vol. 276, no. 5314, pp. 934–937, May 1997.

[8] H. Rott, "The analysis of backscattering properties from SAR data of mountainous regions," *IEEE J. Ocean. Eng.*, vol. OE-9, no. 5, pp. 347–355, Dec. 1984.

[9] R. A. Bindschadler, K. C. Jezek, and J. Crawford, "Glaciological investigations using the synthetic aperture radar imaging system," *Ann. Glaciology*, vol. 9, pp. 11–19, 1987.

[10] H. Rott and C. Maetzler, "Possibilities and limits of synthetic aperture radar for snow and glacier surveying," *Ann. Glaciology*, vol. 9, pp. 195–199, 1987.

[11] M. A. Fahnestock, R. Bindschadler, R. Kwok, and K. C. Jezek, "Greenland ice sheet surface properties and ice dynamics from ERS-1 SAR imagery," *Science*, vol. 262, no. 5139, pp. 1530–1534, Dec. 1993.

[12] K. C. Partington, "Discrimination of glacier facies using multi-temporal SAR data," *J. Glaciology*, vol. 44, no. 146, pp. 42–53, 1998.

[13] R. V. Engeset and D. J. Weydahl, "Analysis of glaciers and geomorphology on svalbard using multitemporal ERS-1 SAR images," *IEEE Trans. Geosci Remote Sens.*, vol. 36, no. 6, pp. 1879–1887, Nov. 1998.

[14] R. V. Engeset, J. Kohler, K. Melvold, and B. Lundèn, "Change detection and monitoring of glacier mass balance and facies using ERS SAR winter images over svalbard," *Int. J. Remote Sens.*, vol. 3, no. 10, pp. 2023–2050, 2002.

[15] R. Storvold, K. A. Hogda, and E. Malnes, "SAR firn line detection and correlation to glacial mass balance; Svartisen glacier, northern Norway," in *Proc. IEEE Int. Geosci. Remote Sens. Symp.*, Anchorage, AK, USA, 2004, pp. 1124–1127.

[16] I. A. Brown, "Synthetic aperture radar measurements of a retreating frn line on a temperate icecap," *IEEE J. Sel. Topics Appl. Earth Observ. Remote Sens.*, vol. 5, no. 1, pp. 153–160, Feb. 2012.

[17] L. Huang, Z. Li, B. Tian, Q. Chen, and J. Zhou, "Monitoring glacier zones and snow/firn line changes in the Qinghai-Tibetan plateau using C-band SAR imagey," *Remote Sens. Environ.*, vol. 137, pp. 17–30, 2013.

[18] V. Akbari, A. Doulgeris, and T. Eltoft, "Monitoring glacier changes using multitemporal multipolarization SAR images," *IEEE Trans. Geosci. Remote Sens.*, vol. 52, no. 6, pp. 3729–3741, Jun. 2014.

[19] P. Rizzoli, M. Martone, H. Rott, and A. Moreira, "Characterization of snow facies on the Greenland ice sheet observed by TanDEM-X interferometric SAR data," *Remote Sens.*, vol. 9, no. 4, 2017, Art. no. 315.

[20] K. C. Jezek, M. R. Drinkwater, J. P. Crawford, R. Bindschadler, and R. Kwowk, "Analysis of synthetic aperture radar data collected over the southwestern Greenland ice sheet," *J. Glaciology*, vol. 38, no. 131, pp. 119–132, 1993.

[21] M. Koenig, J.-G. Winther, N. T. Knudsen, and T. Guneriussen, "Firn-line detection on Austre Okstinbreen, Norway, with airborne multipolarization SAR," *J. Glaciology*, vol. 47, pp. 251–257, Mar. 2001.

[22] E. J. Rignot, "Backscatter model for the unusual radar echoes from the Greenland ice sheet," *J. Geophys. Res.*, vol. 100, no. E5, pp. 9389–9400, May 1995.

[23] J. J. Sharma, I. Hajnsek, K.P. Papathanassiou, and A. Moreira, "Polarimetric decomposition over glacier ice using long-wavelength airborne PolSAR," *IEEE Trans. Geosci. Remote Sens.*, vol. 49, no. 1, pp. 519–534, Jan. 2011.

[24] G. Parrella, I. Hajnsek, and K. Papathanassiou, "Polarimetric decomposition of L-band PolSAR backscattering over the Austfonna ice cap," *IEEE Trans. Geosci. Remote Sens.*, vol. 54, no. 3, pp. 1267–1281, Mar. 2016.

[25] S. Leinss, G. Parrella, and I. Hajnsek, "Snow height determination by polarimetric phase differences in X-band SAR data," *IEEE J. Sel. Topics Appl. Earth Observ. Remote Sens.*, vol. 7, no. 9, pp. 3794–3810, Jun. 2014.

[26] G. Parrella, I. Hajnsek, and K. Papathanassiou, "On the interpretation of polarimetric phase differences in SAR data over land ice," *IEEE Geosci. Remote Sens. Lett.*, vol. 13, no. 2, pp. 192–196, Feb. 2016.

[27] S.R. Cloude, *Polarisation: Applications in Remote Sensing*. London, U.K: Oxford Univ. Press, 2010.

[28] I. Hajnsek, E. Pottier, and S. R. Cloude, "Inversion of surface parameters from polarimetric SAR," *IEEE Trans. Geosci. Remote Sens.*, vol. 41, no. 4, pp. 727–743, Apr. 2003.

[29] S. R. Cloude, J. Fortuny, J. M. Lopez-Sanchez, and A. J. Sieber, "Wideband polarimetric radar inversion studies for vegetation layers," *IEEE Trans. Geosci. Remote Sens.*, vol. 37, no. 5, pp. 2430–2441, Sep. 1999.

[30] S. R. Cloude, D. G. Goodenough, H. Chen, Y. S. Rao, and W. Hong, "Pauli phase calibration in compact polarimetry," *J. IEEE J. Sel. Topics Appl. Earth Observ. Remote Sens.*, vol. 11, no. 12, pp. 4906–4917, Dec. 2018.

[31] C. Mätzler, "Microwave properties of ice and snow," in *Astrophysics and Space Science Library*, B. Schmitt *et al.* Eds. Berlin, Germany: Springer, 1998, pp. 241–257.

[32] R. B. Alley, "The texture of polar firn for remote sensing," *Ann. Glaciol.*, vol. 9, pp. 1–4, 1987.

[33] S. Fujita *et al.*, "Densification of layered firn of the ice sheet at NEEM, Greenland," *J. Glaciology*, vol. 60, no. 223, pp. 905–921, 2014.

[34] E. W. Hoen and H. A. Zebker, "Penetration depths inferred from interferometric volume decorrelation observed over the Greenland ice sheet," *IEEE Trans. Geosci. Remote Sens.*, vol. 38, no. 6, pp. 2571–2583, Nov. 2000.

[35] S. Leinss, H. Loewe, M. Proksch, J. Lemmetyinen, A. Wiesmann, and I Hajnsek, "Anisotropy of seasonal snow measured by polarimetric phase differences in radar time series," *Cryosphere*, vol. 10, pp. 1771–1797, 2016.

[36] S. V. Nghiem, R. Kwok, S. H. Yueh, and M. R. Drinkwater, "Polarimetric signatures of sea ice 1. Theoretical model," *J. Geophys. Res.*, vol. 100, no. C7, pp. 13665–13679, Jul. 1995.

[37] G. Fischer, M. Jaeger, K. P. Papathanassiou, and I. Hajnsek, "Modelling the vertical backscattering distribution in the percolation zone of the Greenland ice sheet with SAR tomography," *IEEE J. Sel. Topics Appl. Earth Observ. Remote Sens.*, vol. 12, no. 11, pp. 4389–4405, Nov. 2019.

[38] M. Pardini, G. Parrella, G. Fischer, and K. Papathanassiou, "A multifrequency SAR tomographic characterization of sub-surface ice volumes," in *Proc. 11th Eur. Conf. Synthetic Aperture Radar*, Hamburg, Germany, 2016, pp. 769–774.

[39] A. W. Nolin and M. C. Payne, "Classification of glacier zones in western Greenland using albedo and surface roughness from the Multi-angle imaging spectro radiometer (MISR)," *Remote Sens. Einvironment*, vol. 107, pp. 264–275, 2007.

[40] M. Koenig, J. Wadham, J. G. Winther, J. Kohler, and A. M. Nuttall,"Detection of superimposed ice on the glaciers kongsvegen and midrelovenbreen, svalbard, using SAR satellite imagery," *Ann. Glaciology*, vol. 34, no. 1, pp. 335–334, Jan. 2002.

[41] S. R. Cloude and E. Pottier, "An entropy based classification scheme for land applications of polarimetric SAR," *IEEE Trans. Geosci. Remote Sens.*, vol. 35, no. 1, pp. 68–78, Jan. 1997.

[42] H. Machguth *et al.*, "Greenland meltwater storage in firn limited by near-surface ice formation," *Nat. Clim. Change*, vol. 6, pp. 390–393, 2016.

[43] M. O. Jeffries, J. Richter-Menge, and J. E. Overland, Eds., Arctic Report Card, 2014. [Online]. Available: http://www.arctic.noaa.gov/reportcard

[44] M. O. Jeffries, J. Richter-Menge, and J. E. Overland, Eds., Arctic Report Card, 2015. [Online]. Available: http://www.arctic.noaa.gov/reportcard

[45] I. Hajnsek, K. Papathanassiou, and S. R. Cloude, "Removal of additive noise in polarimetric eigenvalues processing," in *Proc. IGARSS*, Sydney, Australia, 2001, pp. 2778–2780.

[46] N. Baghdadi *et al.*, "A potential use of C-band polarimetric SAR parameters to characterize the soil surface over bare agricultural fields," *IEEE Trans. Geosci. Remote Sens.*, vol. 50, no. 10, pp. 3844–3858, Oct. 2012.

[47] P. C. J. P. Smeeths *et al.*, "The K-transect in west Greenland: Automatic weather station data (1993-2016)," *Arctic Antarctic Alpine Res.*, vol. 50, no. 1, 2018, Art. no. e1420954.

[48] A. Kovacs, A. J. Gow, and R. M. Morey, "The in-situ dielectric constant of polar firn revisited," *Cold Reg. Sci. Technol.*, vol. 23, no. 3, pp. 245–256, May 1995.